Neural stem cell-derived exosomes promote mitochondrial biogenesis and restore abnormal protein distribution in a mouse model of Alzheimer's disease

Bo Li[1, #], Yujie Chen[2, #], Yan Zhou[1, #], Xuanran Feng[3], Guojun Gu[1], Shuang Han[2], Nianhao Cheng[2], Yawen Sun[1], Yiming Zhang[1], Jiahui Cheng[1], Qi Zhang[4, *], Wei Zhang[1, *], Jianhui Liu[3, *]

https://doi.org/10.4103/1673-5374.385839

Date of submission: March 2, 2023

Date of decision: April 25, 2023

Date of acceptance: August 14, 2023

Date of web publication: September 22, 2023

From the Contents

Graphical Abstract

Neural stem cell derived-exosomes remodel the abnormal distribution of mitochondrial biogenesis-related proteins at the whole-brain level and promote mitochondrial function

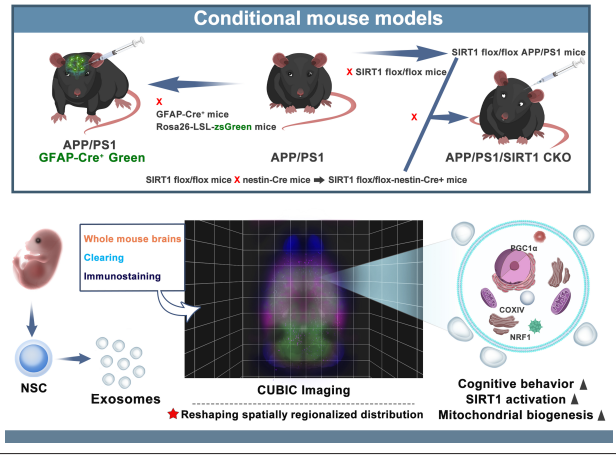

Abstract

Mitochondrial dysfunction is a hallmark of Alzheimer's disease. We previously showed that neural stem cell-derived extracellular vesicles improved mitochondrial function in the cortex of APP/PS1 mice. Because Alzheimer's disease affects the entire brain, further research is needed to elucidate alterations in mitochondrial metabolism in the brain as a whole. Here, we investigated the expression of several important mitochondrial biogenesis-related cytokines in multiple brain regions after treatment with neural stem cell-derived exosomes and used a combination of whole brain clearing, immunostaining, and lightsheet imaging to clarify their spatial distribution. Additionally, to clarify whether the sirtuin 1 (SIRT1)-related pathway plays a regulatory role in neural stem cell-derived exosomes interfering with mitochondrial functional changes, we generated a novel nervous system-SIRT1 conditional knockout APP/PS1 mouse model. Our findings demonstrate that neural stem cell-derived exosomes significantly increase SIRT1 levels, enhance the production of mitochondrial biogenesis-related factors, and inhibit astrocyte activation, but do not suppress amyloid-β production. Thus, neural stem cell-derived exosomes may be a useful therapeutic strategy for Alzheimer's disease that activates the SIRT1-PGC1α signaling pathway and increases NRF1 and COXIV synthesis to improve mitochondrial biogenesis. In addition, we showed that the spatial distribution of mitochondrial biogenesis-related factors is disrupted in Alzheimer's disease, and that neural stem cell-derived exosome treatment can reverse this effect, indicating that neural stem cell-derived exosomes promote mitochondrial biogenesis.

Key Words: Alzheimer's disease; mitochondrial biogenesis; neural stem cell-derived exosome; SIRT1-PGC1α; regional brain distribution; whole brain clearing and imaging

Introduction

Alzheimer's disease (AD), which is a devastating neurodegenerative disorder and the most common form of dementia, is characterized by amyloid plaques, neurofibrillary tangles, and severe neuronal and synaptic loss throughout the brain, resulting in progressive cognitive decline (Lee et al., 2022). Presently, there is no effective therapy available to prevent AD development or reverse AD progression. Accumulation of toxic amyloid-β (Aβ) peptides, which are produced by proteolysis of amyloid precursor protein (APP), is a canonical feature of AD (Donmez et al., 2010, 2021). These Aβ peptides accumulate in mitochondria and subsequently cause mitochondrial dysfunction (Fang et al., 2019; Tracy et al., 2022). Mitochondrial dysfunction increases the level of harmful reactive oxygen species (ROS), decreases mitochondrial ATP production, induces energy deficiency, leads to oxidative damage and synaptic deficits, and eventually results in neuronal loss. Hence, targeting defective mitochondria is an important approach for AD therapy. Sirtuin 1 (SIRT1) is an NAD-dependent deacetylase that modifies several proteins that are crucial for proper mitochondrial function, notably peroxisome proliferator-activated receptor-γ coactivator-1α (PGC1α; Canto et al., 2009; Zhao et al., 2021). Evidence from animal models has shown that SIRT1 exhibits neuroprotective effects in AD through multiple mechanisms, such as inhibiting Aβ plaque production and deposition, suppressing tau hyperphosphorylation, and reducing neuroinflammation (Min et al., 2010; Gomes et al., 2018).

Exosomes, which range in size from 30 to 150 nm in diameter, are essential for intercellular communication and for delivering important proteins and miRNAs that can maintain or alter microenvironmental conditions (Dreyer and Baur, 2016; Thery et al., 2018; Kalluri and LeBleu, 2020; Liu et al., 2022; Jiang et al., 2023). They mediate intercellular communication in many cell types and transfer several kinds of functional biomolecules to affect numerous cellular processes (Montecalvo et al., 2012; Kalluri and LeBleu, 2020). Exosomes originating from multiple cell types have different functions and play varied roles in many of the major physiopathologic pathways that are altered in

[1]Department of Radiology, Renji Hospital, School of Medicine, Shanghai Jiao Tong University, Shanghai, China; [2]Morphology and Spatial Multi-Omics Technology Platform, Shanghai Institute of Nutrition and Health, Chinese Academy of Sciences, Shanghai, China; [3]Department of Anesthesiology, Tongji Hospital, School of Medicine, Tongji University, Shanghai, China; [4]Department of Blood Transfusion, Huashan Hospital, Fudan University, Shanghai, China

*Correspondence to: Qi Zhang, MD, friday0451@163.com; Wei Zhang, MD, zhangwei976@163.com; Jianhui Liu, MD, jianhuiliu_1246@163.com.

https://orcid.org/0000-0002-7330-1811 (Qi Zhang); https://orcid.org/0000-0001-9766-5495 (Wei Zhang); https://orcid.org/0000-0002-8335-0078 (Jianhui Liu)

#These authors contributed equally to this work.

Funding: *This study was supported by the National Natural Science Foundation of China, Nos. 82171194 and 81974155 (both to JL); the Shanghai Municipal Science and Technology Commission Medical Guide Project, No. 16411969200 (to WZ); and Shanghai Municipal Science and Technology Commission Biomedical Science and Technology Project, No. 22S31902600 (to JL).*

How to cite this article: *Li B, Chen Y, Zhou Y, Feng X, Gu G, Han S, Cheng N, Sun Y, Zhang Y, Cheng J, Zhang Q, Zhang W, Liu J (2024) Neural stem cell-derived exosomes promote mitochondrial biogenesis and restore abnormal protein distribution in a mouse model of Alzheimer's disease. Neural Regen Res 19(7):1593-1601.*

AD, such as alleviation of Aβ-induced neurotoxicity (Deng et al., 2021). We recently reported that extracellular vesicles derived from neural stem cells (NSCs) rescue cognitive deficits and improve mitochondrial function in APP/PS1 mice (Li et al., 2020a). However, only the cerebral cortex was investigated, and more research is needed to clarify changes that occur throughout the rest of the brain.

AD-induced cognitive impairment is associated with abnormal energy metabolism in multiple brain regions, such as the hippocampus, cerebral cortex (Frere and Slutsky, 2018; Jagust, 2018), corpus striatum (Li et al., 2022), cerebellum (Wang et al., 2022), basal forebrain (Schmitz et al., 2016), and thalamus (Ryan et al., 2013). Most AD studies have focused on the medial temporal lobe, which contains the hippocampus and the surrounding cortical regions. However, little is known about the mitochondrial metabolic state throughout the whole brain. For decades, histological techniques have been considered the standard procedure for investigating selected tissues, although they have an inherent disadvantage in that they are not able to provide a full picture of the sampled organ, which makes it challenging to compare findings among different individuals. Now, tissue-clearing methods allow 3D imaging of intact organs, with efficient preservation of spatial information. Clear, Unobstructed Brain/Body Imaging Cocktails and Computational analysis (CUBIC) technology enables rapid imaging at the whole-brain level to provide support for multiregional synchronization research (Susaki et al., 2015; Tainaka et al., 2018). Thus, the CUBIC technique can be applied to evaluate alterations in the localization and expression of mitochondrial metabolism-related proteins in AD at the whole-brain level. In this study, we focused on the distribution of mitochondrial biogenesis-related proteins in the brain in mice treated with NSC-derived exosomes (NSC-ex) and explored the pathways involved in NSC-ex-induced changes of these proteins. In addition, considering the important regulatory role of SIRT1 on important mitochondrial biogenesis-related proteins such as PGC-1α, we constructed a nervous system-specific SIRT1 knockout AD-like mouse model to elucidate the role of SIRT1 in regulating NSC-ex-stimulated mitochondrial biogenesis.

Methods

Cell isolation and culture

Mouse hippocampal neurons cells (HT22; Procell, Wuhan, China, Cat# CL-0697, RRID: CVCL_0321) were cultured in Dulbecco's modified Eagle's medium (DMEM) containing 1% 100 μg/mL streptomycin, 10% fetal bovine serum, and 100 U/mL penicillin (all from Thermo Fisher Scientific, Waltham, MA, USA) at 37°C in a 5% CO_2 incubator (Thermo Fisher Scientific). Cells were passaged once every 2–3 days, and cells in logarithmic growth phase were used for subsequent experiments. NSCs (which were used to produce exosomes) were harvested from the hippocampi of ten non-transgenic B6C3 mouse embryos at embryonic day (E) 14, as we previously described (Li et al., 2020a), and cultured in neurobasal medium supplemented with 2% B27, human recombinant epidermal growth factor (EGF, 20 ng/mL; Gibco, Grand Island, NY, USA), basic fibroblast growth factor (bFGF; 20 ng/mL; Gibco), and heparin (5 μg/mL; Sigma, St. Louis, MO, USA).

Exosome isolation and identification

The culture supernatants of NSCs were collected for isolating exosomes, referring to previous protocols (Rong et al., 2019; Li et al., 2020a; Pan et al., 2020). Briefly, the growth medium was collected, and dead cells, cellular debris, and larger microvesicles were removed by sequential centrifugation (300 × *g* for 10 minutes, followed by 1000 × *g* for 10 minutes and 20,000 × *g* for 30 minutes at 4°C) and filtration through a 0.22-μm filter (Millipore, Burlington, MA, USA). The total concentration of exosomes was determined using a bicinchoninic acid (BCA) kit (Sigma). NSC-ex morphology was assessed using a transmission electron microscope (Philips CM 120; Philips, Amsterdam, Netherlands). The size distribution of the exosomes was analyzed by nanoparticle tracking analysis, as we described previously (Li et al., 2020a). Furthermore, the exosome-specific markers CD63 (1:1000, Abcam, Cambridge, UK, Cat# ab217345, RRID: AB_2754982), Alix (1:1500, Abcam, Cat# ab117600), Flotillin1 (1:10,000, Abcam, Cat# ab133497, RRID: AB_11156367), and TSG101 (1:2000, Abcam, Cat# ab125011, RRID: AB_10974262) were detected by western blot analysis, and Calnexin (1:2000, Abcam, Cat# ab133615, RRID: AB_2864299) was detected as a negative control.

In vitro assessment

HT22 cells were used for *in vitro* experiment. The cells were divided into groups as follows: negative control, control, $A\beta_{25–35}$ (25 μmol), and $A\beta_{25–35}$ + NSC-ex. After the cells had been treated as indicated by their group assignment, they were washed in PBS containing 1% BSA and resuspended to a final cell concentration of 1 × 10^5/mL. No primary antibodies were added to the negative control tube, while an anti-SIRT1 (mouse, Abcam, Cat# ab110304, RRID: AB_10864359) antibody or anti-peroxisome proliferator-activated receptor-γ coactivator-1α (PGC1α; rabbit, Abcam, Cat# ab54481, RRID: AB_881987) antibody was added to the tubes containing the samples to be tested (diluted 1:200 in phosphate buffered solution [PBST]). The solutions were mixed thoroughly and incubated for 60 minutes at room temperature. After the cells were washed and resuspended again, secondary antibodies-Cy3 goat anti-mouse IgG (ABclonal, Wuhan, Hubei Province, China, Cat# AS008, RRID: AB_2769088) and ABflo® 647 F(ab')2 Fragment goat anti-rabbit IgG (ABclonal, Cat# AS086) were added. According to the manufacturer's instructions, the cells were incubated with the secondary antibodies for 20 minutes at room temperature with shaking in the dark. Then, cell washing solution was added to the tubes, which were centrifuged at 200 × *g* for 5 minutes, after which the supernatant was discarded and the cells were washed another two times. Finally, the cells were resuspended in 100–200 μL of cell wash solution for test. Flow cytometry (Beckman, Brea, CA, USA) was used to detect the fluorescence intensity of the samples. The flow cytometry data were analyzed using Cytexpert (Beckman). HT22 cells were seeded and cultured overnight for mitochondrial membrane potential (MMP) detection. The cells were divided into three groups: control, $A\beta_{25–35}$ (25 μmol), and $A\beta_{25–35}$ + NSC-ex. After being treated according to their group assignment, the cells were washed with PBS and then incubated with 5,5′,6,6′-tetrachloro-1,1′,3,3′-tetra-ethyl benzimidazolyl carbocyanine iodide (JC-1) fluorescent dye (C2003S, Beyotime, Shanghai, China) for 20 minutes at 37°C. After removing the dye and washing with PBS washing, red/green fluorescence was detected using a confocal laser scanning microscope (LSM710, Carl Zeiss, Oberkochen, Germany) according to the manufacturer's instruction.

Animals

Two transgenic (Tg) mouse models were used in this study. The first was APP/PS1 GFAP-Cre^+ Green mice (hereafter referred to as AD mice) generated by cross-breeding APP/PS1 mice, also known as B6C3-Tg (APPswe, PSEN1dE9) 85Dbo/J mice (Stock No. 34829, The Jackson Laboratory, Bar Harbor, Maine, USA), with glial fibrillary acidic protein (GFAP)-Cre^+ mice (FVB-Tg[GFAP-cre]25Mes/J, Stock No. 004600, The Jackson Laboratory) and rosa26-LSL-zsGreen mice (Stock No. NM-KI-200045, Shanghai Model Organisms Center, Inc., Shanghai, China). The second was a novel Tg mouse constructed as follows: $SIRT1^{co/co}$ mice (B6;129-$Sirt1^{tm1Ygu}$/J, Stock No. 008041, The Jackson Laboratory), nestin-Cre mice (Stock No. 003771, The Jackson Laboratory), and APP/PS1 mice (Stock No. 34829, The Jackson Laboratory) were obtained from Jackson Laboratory. Nervous system-specific SIRT1 knockout ($SIRT1^{flox/flox}$-nestin-Cre^+) mice were generated by crossing $SIRT1^{flox/flox}$ mice with nestin promoter-driven Cre (nestin-Cre) mice. $SIRT1^{flox/flox}$ mice were crossed with APP/PS1 mice to generate $SIRT1^{flox/flox}$ APP/PS1 mice. Finally, nervous system-specific SIRT1 conditional knockout APP/PS1 (APP/PS1/SIRT1 CKO [hereafter referred to as SKO-AD]) mice were generated by crossing $SIRT1^{flox/flox}$-nestin-Cre^+ mice with $SIRT1^{flox/flox}$ APP/PS1 mice. Wild-type (WT) control mice (from Jackson Laboratory) were of the same genetic background as the AD mice, and, where relevant, Cre^+ mice were included to account for the effects of Cre (no adverse effects due to Cre expression itself were observed *in vitro* or *in vivo*). All experimental mice were 9-month-old males weighing 20–25 g, with no obvious physical defects. We chose to use exclusively male mice because males have better physical health indicators than females, which can reduce experimental contingencies to a certain extent. All animal protocols were verified by the Shanghai Model Organisms Center, Inc. (Shanghai, China). All experimental animal procedures and animal care were approved by the Animal Ethics Committee of Tongji Hospital of Tongji University (approval No. 2021-DW-SB-026, November 4, 2021). These mice were housed in separate cages with a 12/12-hour light/dark cycle (7:00 a.m. to 7:00 p.m.), and food and water were available ad libitum. Several measures were taken to minimize animal discomfort, such as administration of cefradine to prevent infection after surgery.

Animal groups

The mice were randomly divided into five experimental groups: non-Tg mice WT littermates left untreated (WT group, *n* = 15), SKO-AD mice injected with phosphate-buffered saline (PBS) (SKO-AD-Veh group, *n* = 15), AD mice injected with vehicle (AD-Veh group, *n* = 15), SKO-AD mice injected with NSC-derived exosomes (SKO-AD-ex group, *n* = 15), and AD mice injected with NSC-derived exosomes (AD-ex group, *n* = 15). AD mice or SKO-AD mice were randomly assigned to the relevant groups using a simple randomization method, as previously described (Li et al., 2020a). No mice were excluded from the data analysis.

Exosome delivery

Using mouse brain stereotaxic coordinates (Zhang et al., 2013), NSC-ex were bilaterally injected into the lateral ventricles at the following coordinates: anteroposterior, –0.22 mm; mediolateral, –1.00 mm; dorsoventral, –2.30 mm relative to the bregma. The specific stereotactic delivery process was performed as previously detailed (Li et al., 2020a). Mice were deeply anesthetized (tribromoethanol, 500 mg/kg body weight, intraperitoneal injection; Sigma) and placed in a stereotaxic apparatus (RWD, Shenzhen, Guangdong Province, China). For each group, 200 μg (10 μL) of either NSC-ex or equivoluminal PBS were injected at a flow rate of 1 μL/min over a period of 5 minutes (David Kopf Instruments, Tujunga, CA, USA). The syringe was allowed to remain in the injection site for another 5 minutes to allow diffusion into the surrounding tissues. Injections were given twice each week for 4 weeks, and cefradine was applied to surgical wounds after the surgery.

Behavioral assessment

Five weeks after exosome/vehicle delivery (mice age: 11.5 months), ten mice from every group of similar weights were selected for assessment in the Morris water maze (MWM; Mobile Datum Information Technology Co., Ltd., Shanghai, China), which is used to evaluated spatial learning and memory, as described in detail in our earlier studies (Li et al., 2018, 2020a). The evaluator was blinded to the group assignments. The swimming paths and speed of the mice in the examined groups were recorded using a computerized video imaging analysis system (Shanghai Mobile Datum Information Technology Co., Ltd.). The MWM training phase included a navigation test and a spatial probe test. Learning ability was evaluated through the navigation test over 6 days to record escape latency. Each mouse was given up to 60 seconds to search for the platform. The spatial probe test was performed at 5:00 p.m. on the 7^{th} day

to evaluate memory retention. Frequency of crossing over the platform, time spent in the target quadrant (TQ), and time spent in the other quadrants were recorded.

Immunostaining of whole mouse brains

After the behavioral tests were finished, the mice were euthanized with a lethal dose of pentobarbital sodium (5%, 250 mg/kg, Sigma) via intraperitoneal injection and perfused with 4% paraformaldehyde (PFA) in PBS in a fume hood. The whole brain, including cerebrum, cerebellum, and olfactory bulb, was removed from the skull, washed with 1×PBS, transferred to Clear, Unobstructed Brain/Body Imaging Cocktails and Computational analysis (CUBIC) 1 solution (25 wt% urea and 25 wt% N,N,N',N'-tetrakis (2-hydroxypropyl) ethylenediamine, 15 wt% polyethylene glycol mono-p-isooctylphenyl ether/Triton X-100 in appropriate distilled water) and dried in a 37°C oven for approximately 10 days (Tomer et al., 2014; Susaki et al., 2015). The solution was changed every 3 days until the entire brain was transparent.

The brains were then washed with 1×PBS for 2 hours at room temperature, then overnight, and for another 2 hours, followed by incubation with DAPI (Sigma, Cat# D9542) and primary antibody solutions containing 0.2% sodium azide and 0.5% Triton-X100 for 7 days on a rotator at 37°C. The primary antibodies included anti-PGC1α (rabbit, Abcam, Cat# ab54481, RRID: AB_881987), anti-nuclear respiratory factor 1 (NRF1) (rabbit, Abcam, Cat# ab200976; Alexa Fluor® 488), anti-NRF1 (rabbit, Abcam, Cat# ab200979; Alexa Fluor® 647), and anti-cytochrome C oxidase IV (COXIV) (rabbit, Abcam, Cat# ab210675; Alexa Fluor® 555). These primary antibodies were incubated for 7 days at 37°C. All of the brains were stained with both an anti-NRF1 antibody and the anti-COXIV antibody. The brains were subsequently washed with PBST several times and incubated with secondary antibody (donkey anti-rabbit IgG [1:50, Thermo Fisher Scientific]) for 4 days on a rotator at 37°C. Next, the tissues were repetitively washed and then immersed in 20% sucrose-PBS. Finally, the brains were immersed in 1/2 CUBIC 2 solution overnight, then immersed in CUBIC 2 solution until they became transparent again (Susaki et al., 2015). The CUBIC 2 solution is a mixture of 10% (w/v) 2,2',2''-nitrilotriethanol, 50% (w/v) sucrose, 25% (w/v) urea, and 0.1% (v/v) Triton X-100.

Whole-brain imaging

Whole-brain images were acquired with a Zeiss Z.1 light sheet microscope (Carl Zeiss) using a 5× objective and 488-nm, 555-nm, and 647-nm laser light sheets. Z-stacks were created by optically sectioning samples during imaging, and sample fluorescence was imaged with a PCO Edge 5.5 camera (Excelitas PCO GmbH, Kelheim, Germany) to generate each z-plane, with sequential excitation of the samples using left- and right-orientated light sheets. The sequential images were merged using Zen light sheet software (Zeiss) to create a single fluorescent image for each z-plane. The brains were scanned with z-step size of 10 µm. 3D reconstruction was achieved using Arivis Vision 4 dimensional (4D) software (arivis AG, Rostock, Germany), and screenshots were taken.

Fluorescence signal intensity analysis

To better visualize and analyze the acquired 3D whole-brain fluorescence data, all 2D fluorescence images contained in the 3D views were exported for further semi-quantitative analysis, which the background signal suppressed as much as possible. The 2D fluorescence images were then analyzed using ImageJ (version 1.53e, National Institutes of Health, Bethesda, MD, USA) (Schneider et al., 2012). Considering the large number of images, the increment was set to twenty, i.e., every twenty images were combined into a single image. Next, 50 regions of interest were randomly selected for each specific brain region for measurement of the fluorescence signal value, and then the levels of related factors in different brain regions were semi-quantified based on the average fluorescence signal intensity. The selected brain regions included the hippocampus, striatum, medial cortex, lateral cortex, thalamus, hypothalamus, midbrain, cerebellum, and brainstem.

Western blotting

Five mice from each group were euthanized and used to prepare samples for western blotting (WB). Protein extraction from different brain regions (corpus striatum, hippocampus, cortex, and cerebellum) and western blotting were carried out as described previously (Li et al., 2020a). The extracted proteins from each group were separated by 15% sodium dodecyl sulfate-polyacrylamide gel electrophoresis and transferred to polyvinylidene fluoride membranes (Sigma). Specific antibodies were used to detect CD63, ALIX, Flotillin1, TSG101, Calnexin, SIRT1, PGC1α, NRF1 (rabbit, 1:2000, Abcam, Cat# ab175932, RRID: AB_2629496), COXIV (rabbit, 1:1000, Thermo Fisher Scientific, Cat# PA5-29992, RRID: AB_2547466), and GAPDH (1:1000, Cell Signaling Technology). The primary antibodies were incubated overnight at 4°C. Donkey anti-mouse IgG (Cat# SA1-100, RRID: AB_325993; 1:500, Thermo Fisher Scientific) and donkey anti-rabbit IgG (Cat# SA1-200, RRID: AB_325994; 1:300, Thermo Fisher Scientific) were used as secondary antibodies. The membranes were incubated with the secondary antibodies for 2 hours at 37°C. Densitometric band analysis was carried out using a KS 400 image analysis system (version 3.0; Carl Zeiss, Germany).

Enzyme-linked immunosorbent assay

Five mice from each group were randomly selected for enzyme-linked immunosorbent assay (ELISA). First, 3–6 µL cerebrospinal fluid and 1 mL peripheral blood (PB) were extracted from each mouse, as previously reported, with minor modifications (Qiao et al., 2016). Levels of soluble and insoluble amyloid-β (i.e. $Aβ_{40}$, $Aβ_{42}$, and the ratio of $Aβ_{42/40}$) in the cerebrospinal fluid and serum were quantified as previously described (Zhang et al., 2016). Briefly, the total Aβ concentration in each sample was determined by quantitative sandwich ELISA (Immuno-Biological Laboratories, Co., Ltd., Gunma, Japan) following the manufacturer's instructions, carried out in duplicate, and then absorbance at 450 nm was measured using an ELISA reader (Multiskan EX; Labsystem, Helsinki, Finland). The samples were coded prior to performing the assays.

Statistical analysis

All experiments were performed by evaluators blinded to the group assignments who collected, calculated, and analyzed the data. Data from each experiment were normally distributed, as determined by Shapiro-Wilk test, and are presented as mean ± standard deviation (SD). Outliers was tested via boxplot in SPSS (version: 26.0.0.0, IBM, Armonk, New York, USA). Ultimately, no data were excluded from the analysis. Data were analyzed using two-way analysis of variance or repeated-measures analysis of variance with the least significant difference *post hoc* test. A *P*-value < 0.05 was considered statistically significant.

Results

Verification of NSC-ex and SKO-AD mouse model

We previously showed that extracellular vesicles derived from NSCs stimulate the secretion of several important regulators of mitochondrial function in the cortex of mice. To further explore the impact of NSC-ex, as well as SIRT1, on mitochondrial biogenesis we generated a novel nervous system-specific SIRT1 conditional knockout APP/PS1 mouse model and conducted a series of experiments using this model, together with APP/PS1 GFAP-Cre^{+} Green mice. NSC-ex were isolated by ultracentrifugation (Chen et al., 2018a, b; Pan et al., 2020) and appeared as round, cup-shaped particles 30–150 nm in diameter with a double-layer membrane structure by TEM (**Figure 1A**), consistent with an earlier report (van Niel et al., 2018). The identity of the NSC-ex was also confirmed by nanoparticle tracking analysis (**Figure 1C**), as well as immunoblotting analysis with the negative marker Calnexin and the canonical exosome-related markers CD63, Alix, Flotillin 1, and TSG101 (**Figure 1B**). Successful construction of the SKO-AD mouse model was confirmed by the absence of SIRT1 mRNA and protein expression in the brain (**Additional Figure 1**).

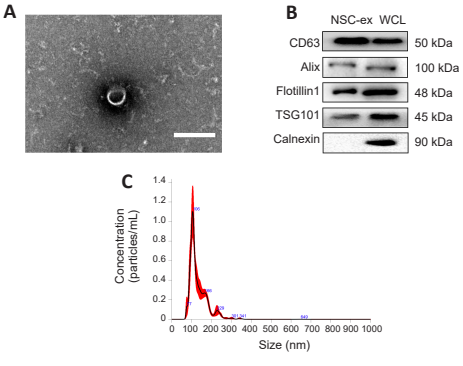

Figure 1 | **Characterization of NSC-ex.**
(A–C) Representative transmission electron microscopy images of NSC-ex (A), western blotting (canonical exosome-related markers CD63, Alix, Flotillin 1, and TSG101; a negative marker Calnexin) (B), and nanoparticle tracking analysis (C). Scale bar: 200 nm. NSC-ex: Neural stem cell-derived exosomes.

NSC-ex reverse cognitive impairments in two AD mouse models

Behavioral assessment was carried out using the MWM. In the navigation test, WT and AD-ex mice exhibited significantly shorter escape latencies and swimming distances during days 3–6 of training than SKO-AD-Veh, SKO-AD-ex, and AD-Veh mice (n = 10, P < 0.01; **Figure 2A** and **B**), indicating that there were significant cognitive deficits in these three groups and that treatment with NSC-ex successfully improved spatial learning ability in AD mice. The AD-ex group exhibited dramatically shorter escape latencies from day 2 to 6 than the SKO-AD-ex group (n = 10, P < 0.001; **Figure 2A**), and similar results were observed in the AD-Veh group *vs*. the SKO-AD-Veh group, clearly demonstrating that nervous system-specific SIRT1 knockout resulted in much more severe cognitive disorder. In addition, the SKO-AD-ex group exhibited significantly shorter escape latencies during days 3–6 compared with the SKO-AD-Veh group (n = 10, P < 0.01; **Figure 2A**), while the swimming distances were only shorter on days 4 and 5 (n = 10, P < 0.05; **Figure 2B**). This demonstrates that treatment with NSC-ex can rescue spatial learning deficits in SKO-AD mice, but not to the same extent as in AD mice. Another point worth noting is that the speed of the SKO-AD-Veh mice was slightly lower than that of the other four groups to varying degrees, indicating that the aggravated behavioral symptoms of SKO-AD mice have reached to movement disturbance, though this was improved by treatment with NSC-ex (n = 10; **Figure 2C**).

In the spatial probe test, the mice in the AD-ex group showed significantly more crossings and spent more time in the target quadrant than the mice in the AD-Veh group (n = 10, P < 0.01; **Figure 2D** and **E**), suggesting that treatment with NSC-ex restored memory. SKO-AD-ex mice spent more time in the target quadrant than SKO-AD-Veh mice (n = 10, P < 0.05; **Figure 2E**). However, there was only a slight increase in the number of crossings made by mice in the SKO-AD-ex group compared with that made by mice in the SKO-AD-Veh group (n = 10, P > 0.05; **Figure 2D**), and both counts were lower than those in the AD groups (**Figure 2D**). In addition, the amount of time spent in the target quadrant by mice in the WT and AD-ex groups was significantly greater than the amount of time spent in the other three quadrants (n = 10, P < 0.001; **Figure 2F**), while there was no significant difference between the SKO-AD-Veh and AD-Veh groups (n = 10, P > 0.05; **Figure 2F**). Mice in the SKO-AD-ex group also spent more time in the target quadrant than in the other quadrants (n = 10, P < 0.05; **Figure 2F**). Taken together, these findings indicate that NSC-ex ameliorate the spatial learning and memory impairments caused by AD. Moreover, the absence of SIRT1 expression exacerbated cognitive impairment and cut down the beneficial effects of NSC-ex treatment in the SKO-AD groups.

NSC-ex show only a slightly positive effect on Aβ levels

AD is characterized by extracellular deposition of Aβ, a 39–43 amino acid peptide derived from APP by β- and Ɣ-secretase cleavage. $Aβ_{1–40}$ and $Aβ_{1–42}$ are the major components of vascular amyloid deposits (Donmez et al., 2010; Tatulian, 2022). Anti-Aβ immunotherapies consistently rescue cognitive deficits in many transgenic AD models. To determine whether NSC-ex have a beneficial effect on β-amyloidosis, we measured levels of both soluble and insoluble $Aβ_{40}$ and $Aβ_{42}$ in the brain by ELISA. The soluble and insoluble Aβ levels in the SKO-AD group were significantly higher than those in the AD group, indicating that nervous system-specific SIRT1 knockout exacerbates Aβ deposition. Unexpectedly, NSC-ex treatment did not result in significant clearance of soluble and insoluble Aβ in the SKO-AD and AD groups (n = 5, P > 0.05; **Figure 2G** and **H**). However, there was a significant decrease in the ratio of soluble $Aβ_{42}$ to $Aβ_{40}$ in the SKO-AD groups (n = 5, P < 0.05; **Figure 2G**), demonstrating that NSC-ex have a slightly positive effect on Aβ levels. However, there was no significant difference in the ratio of $Aβ_{42}$ to $Aβ_{40}$ among the other groups. Overall, these findings indicate that NSC-ex rescued cognitive deficits in AD mouse models without distinctly altering Aβ burden, suggesting that NSC-ex do not function primarily by reducing Aβ deposition. Thus, we speculated that the beneficial effects of NSC-ex might be mediated by changes in mitochondrial function.

NSC-ex activate SIRT1 and increase the levels of mitochondrial biogenesis-related proteins in multiple brain regions

Mitochondrial damage is an early event in AD pathogenesis. PGC1α, NRF1, and COXIV are all crucial mitochondrial biogenesis-related factors. PGC1α, a transcriptional regulatory factor, activates gene transcription, protects neurons from oxidative damage, promotes ATP production during bioenergetic crises, maintains energy homeostasis, and prevents cell necrosis and apoptosis (Rius-Perez et al., 2020). NRF1 is a transcriptional partner of PGC1α and controls the expression of mitochondrial transcription factor A, which is vitally important for regulating DNA replication and the transcription of mitochondrial genes (Liu et al., 2021). COXIV, a protein that is specifically expressed in mitochondria, is an indirect indicator of mitochondrial biogenesis, and defective COXIV protein expression have been found senile plaques in patients with dystrophic neuritis or AD (Perez-Gracia et al., 2008; Zhou et al., 2023). We first asked whether there was a correlation between SIRT1 and PGC1α expression levels after NSC-ex treatment *in vitro*. We found that the fluorescence intensities of SIRT1 and PGC1α were significantly lower in the $Aβ_{25–35}$-treated group and dramatically higher after NSC-ex treatment (**Figure 3A** and **B**). Next, we assessed the mitochondrial membrane potential (MMP), which is an indicator of intracellular homeostasis and mitochondrial energy status. $Aβ_{25–35}$ infiltration into HT22 cells stimulated massive JC-1 green fluorescence, indicating MMP loss (**Figure 3C**). NSC-ex improved the MMP performance, indicating that NSC-ex preserve mitochondrial function.

Next, we performed WB to determine the expression levels of proteins related to mitochondrial biogenesis in the corpus striatum, cerebral cortex, hippocampus, and cerebellum of AD mice. As expected, the protein levels of PGC1α, NRF1, and COXIV in the four brain regions from mice in the AD-Veh group were significantly lower than those in WT mice (n = 5, P < 0.001; **Figure 4A–D**), demonstrating that AD severely impairs mitochondrial biogenesis. Compared with those in the AD-Veh group, the protein levels of PGC1α, NRF1, and COXIV in the AD-ex group were significantly increased in the striatum, hippocampus, and cortex (n = 5, P < 0.05; **Figure 4A–C**). In particular, the levels of PGC1α in the cortex and hippocampus and of NRF1 in the hippocampus in the AD-ex group were nearly equal to or slightly higher than those seen in the WT group, suggesting a stronger endogenous response to NSC-ex-induced mitochondrial biogenesis. As described earlier, behavioral assessment showed that SKO-AD mice had markedly worse cognitive impairment than AD mice, and the WB results revealed that PGC1α, NRF1, and COXIV expression levels in the four braing regions were significantly lower after nervous system-specific SIRT1 knockout (n = 5, P < 0.01; **Figure 4A–D**, SKO-AD-Veh group *vs*. AD-Veh group), indicating that SIRT1 deletion further impedes mitochondrial biogenesis. Similarly, SKO-AD-ex mice showed significantly higher levels of PGC1α, NRF1, and COXIV than SKO-AD-Veh mice in the striatum, hippocampus, and cortex (n = 5, P < 0.05; **Figure 4A–C**), indicating that NSC-ex can promote mitochondrial biogenesis through SIRT1-independent pathways. This might explain why NSC-ex ameliorated the reduced mobility seen in the SKO-AD-Veh group. Treatment with NSC-ex significantly increased the PGC1α level in the cerebellum (n = 5, P < 0.01; **Figure 4D**, AD-ex group *vs*. AD-Veh group, SKO-AD-ex group *vs*. SKO-AD-Veh group), while there was no apparent increase in NRF1 or COXIV expression (n = 5, P > 0.05; **Figure 4D**).

Given that NSC-ex treatment stimulated PGC1α production in the hippocampus and cortex, we also detected alterations in SIRT1 levels in these two regions. The WB results showed that treatment with NSC-ex significantly promoted SIRT1 activation in the hippocampus and cortex, and that SIRT1 expression in the hippocampus was significantly higher in the AD-ex group than in the WT group (n = 5, P < 0.001; **Figure 4E**). No SIRT1 expression was observed in the SKO-AD-ex group. Expression of both SIRT1 and PGC1α was clearly increased in the hippocampus. Overall, our data show that NSC-ex improve mitochondrial biogenesis in multiple brain regions, and that the SIRT1-PGC1α pathway is very important to this process.

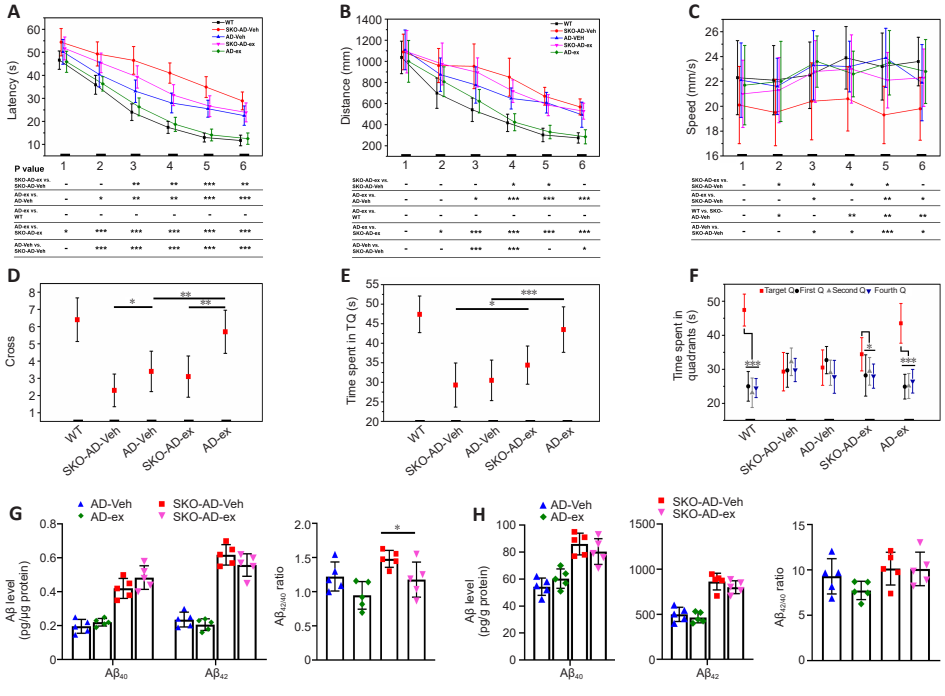

Figure 2 | NSC-derived exosomes rescue cognitive deficits in AD mouse models without significantly reducing Aβ burden.
(A and B) The escape latencies and swimming distances of mice in the five groups in the navigation test (n = 10). (C) The swimming speed of mice in the five groups (n = 10). (D and E) The number of crossings and time spent in the target quadrant for each group in the spatial probe test (n = 10). (F) Time spent in the target quadrant and the other three quadrants (n = 10). (G and H) Quantification of soluble (G) and insoluble (H) Aβ peptide levels (n = 5). Error bars indicate mean ± SD. n = number of animals. *P < 0.05, **P < 0.01, ***P < 0.001 (repeated-measures analysis of variance or two-way analysis of variance with the least significant difference *post hoc* test). The mice were randomly divided into five experimental groups: non-Tg mice WT littermates left untreated (WT group), SKO-AD mice injected with phosphate-buffered saline (PBS) (SKO-AD-Veh group), AD mice injected with vehicle (AD-Veh group), SKO-AD mice injected with NSC-derived exosomes (SKO-AD-ex group), and AD mice injected with NSC-derived exosomes (AD-ex group). AD: Alzheimer's disease; Aβ: amyloid-β; NSC: neural stem cell.

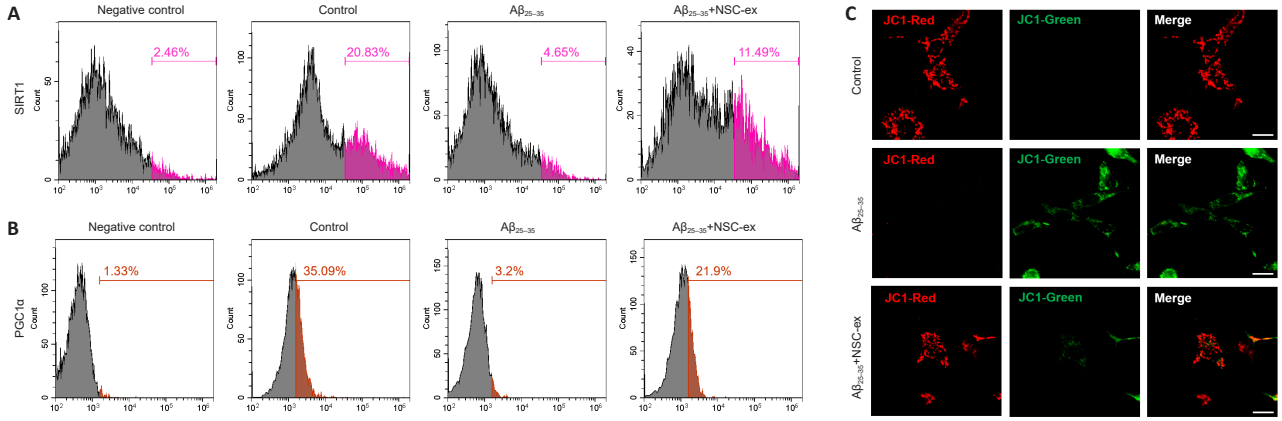

Figure 3 | **NSC-ex promote SIRT1 and PGC1α secretion and improve mitochondrial function in an Aβ-induced HT22 cell injury model.**
(A and B) Detection of SIRT1 (A) and PGC1α (B) in the four groups of HT22 cells as detected by flow cytometry. (C) Mitochondrial membrane potential in each group, as detected by staining mitochondria with JC-1 and viewing the cells using a confocal microscope (n = 3). Free JC-1 monomers in mitochondria exhibit green fluorescence, and JC-1 aggregates exhibit red fluorescence. A decrease in red fluorescence and an increase in green fluorescence imply mitochondrial depolarization. Scale bars: 20 μm. Aβ: Amyloid-β; NSC-ex: neural stem cell-derived exosomes; PGC1α: proliferator-activated receptor-γ coactivator-1α.

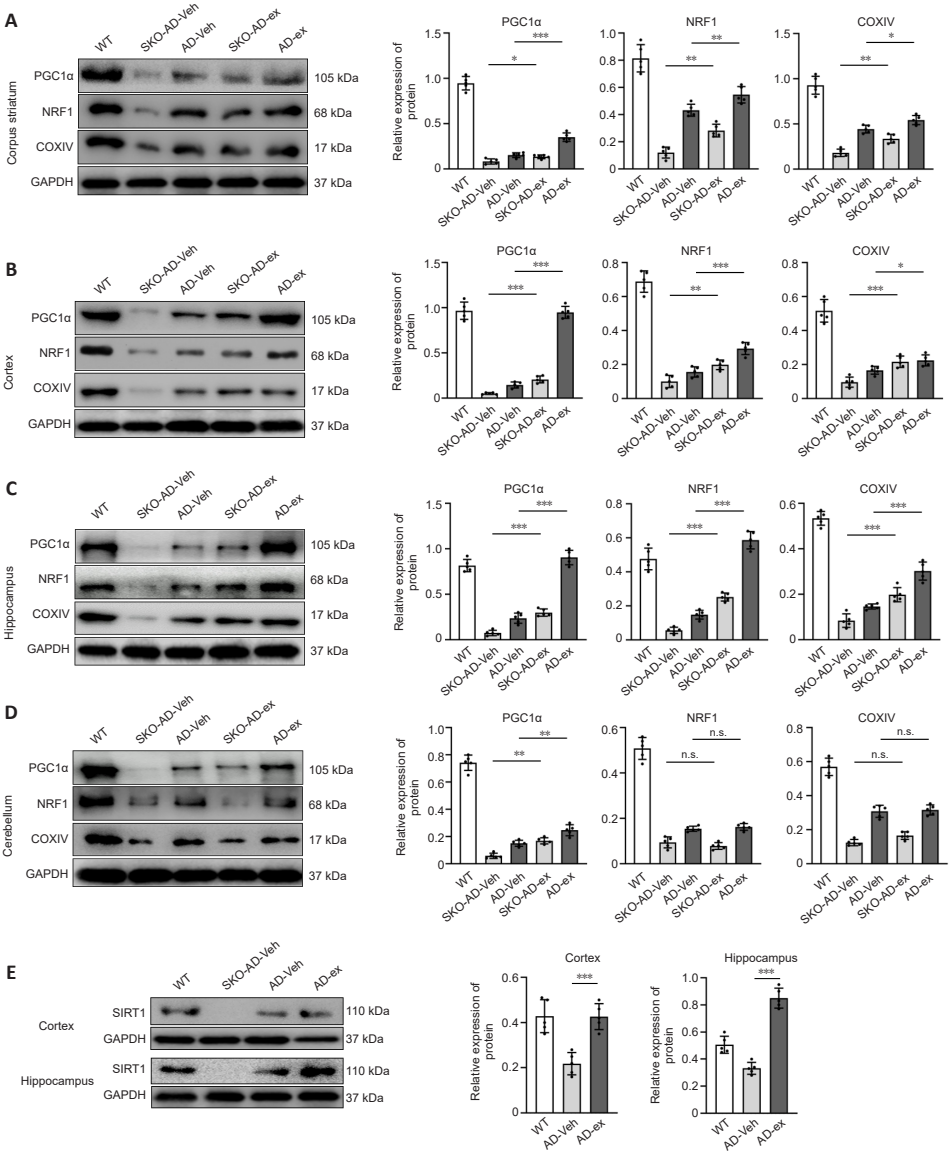

Figure 4 | **NSC-ex increase the protein levels of mitochondrial biogenesis-related factors and SIRT1 in multiple brain regions.**
(A–D) WB evaluation of PGC1α, NRF1, and COXIV levels in the corpus striatum (A), cortex (B), hippocampus (C), and cerebellum (D; n = 5 animals). (E) WB evaluation of SIRT1 levels in the hippocampus and cortex (n = 5 animals). Error bars indicate mean ± SD. *P < 0.05, **P < 0.01 and ***P < 0.001 (one-way analysis of variance with the least significant difference *post hoc* test). The mice were randomly divided into five experimental groups: non-Tg mice WT littermates left untreated (WT group), SKO-AD mice injected with phosphate-buffered saline (PBS) (SKO-AD-Veh group), AD mice injected with vehicle (AD-Veh group), SKO-AD mice injected with NSC-derived exosomes (SKO-AD-ex group), and AD mice injected with NSC-derived exosomes (AD-ex group). AD: Alzheimer's disease; Aβ: amyloid-β; COX IV: cytochrome C oxidase IV; GAPDH: glyceraldehyde 3-phosphate dehydrogenase; NFR: nuclear respiratory factor 1; NSC-ex: neural stem cell-derived exosomes; n.s.: not significant; NSC: neural stem cell; PGC1α: proliferator-activated receptor-γ coactivator-1α; SIRT1: sirtuin 1; WB: western blotting.

NSC-ex reverse abnormal PGC1α distribution in the brain in an AD mouse model

2D immunofluorescence is typically used to detect changes in the distribution of proteins in tissues of interest, but is limited by the need to perform multiple sets of same operations simultaneously, the inability to control some experimental details, and the inability to detect holistic differences. Here, we used whole-brain clearing, immunostaining, and lightsheet imaging to investigate the distribution of PGC1α, NRF1, and COXIV at the whole-brain level. **Additional Video 1** shows a representative view of PGC1α and GFAP fluorescence in the AD-Veh group. To better display the spatial distributions of these factors in the mouse brains, three angles of the 3D images are presented here, namely the transverse angle (**Figure 5Da**), the coronal angle with the head end 30 degrees upwards (**Figure 5Db**), and the side angle (**Figure 5Dc**). Negative controls were included to ensure the authenticity and specificity of the fluorescence signal, and no obvious fluorescence was observed in the negative controls (**Additional Figure 2**). Overall distribution trends were determined based on a combination of 3D viewer and corresponding 2D images to identify specific fluorescence signals.

In general, we found that PGC1α was diffusely and abundantly distributed throughout the brain of WT mice (**Figure 5Aa** and **b**, **Bg**). Fluorescence signal intensity analysis (**Figure 5E**) indicated slightly higher PGC1α expression in the hippocampal, cortical, and striatal regions, and no obvious regions of hypo-fluorescence. Representative enlarged images of the hippocampus (**Additional Figure 3h1–h4**), corpus striatum (**Additional Figure 3s1** and **s2**), thalamus (**Additional Figure 3t1**), midbrain (**Additional Figure 3m1**), cortex (**Additional Figure 3s2**, **o1** and **c2**), and cerebellum (**Additional Figure 3c1**) are shown. However, unlike the WT group, brains from both the AD-Veh group (**Figure 5Ac** and **d**, **5Bh**) and the AD-ex group (**Figure 5Ae** and **f**, **Bi**) showed markedly heterogeneous distribution of PGC1α, especially the AD-Veh group. Compared with that of WT mice, the whole-brain PGC1α fluorescence intensity of AD-Veh mice (**Figure 5F**) was significantly lower, and the distribution of PGC1α was altered, indicating that PGC1α expression decreased differentially in multiple brain regions, most notably in the hippocampus, cortex, thalamus and brainstem. This finding is consistent with the WB results. After NSC-ex treatment, we observed markedly increased PGC1α expression levels in multiple brain regions, including the striatum (**Figure 5Cj**), cortex (**Figure 5Ck** and **l**), hippocampus (**Figure 5Cm**), cerebellum (**Figure 5Cn**), midbrain (**Figure 5Co**), and more. PGC1α distribution was severely disrupted in AD mouse brains (**Figure 5Ac** and **d**, **Bh**), but less so in brains from the AD-ex group (**Figure 5Ae** and **f**, **Bi**). The fluorescence intensity results (**Figure 5F** and **G**) revealed that the regions with the most pronounced increase in PGC1α expression in the AD-ex group were hippocampus and cortex, which is also consistent with the WB results. Interestingly, the decrease in PGC1α expression from the inner to the outer layer of the cortex of WT group was very slight (**Figure 5Ck** and **l** [WT group]), whereas treatment with NSC-ex tended to drastically increase PGC1α expression in the medial cortex (**Figure 5Ck** and **l** [AD-ex group]). Taken together, our findings demonstrate that AD disrupts normal PGC1α distribution in the brain, and that NSC-ex reverse this effect in multiple brain regions.

NSC-ex restore normal NRF1 and COXIV distribution patterns

NRF1 and COXIV fluorescence signals were detected simultaneously in mouse brains. Combining 3D views and fluorescence signal intensity analysis showed that NRF1 and COXIV were abundantly expressed in WT mice, and their spatial distributions overlapped substantially (**Figure 6Aa–d**, **B**, and **G**). Compared with those in the WT group, NRF1 and COXIV expression levels were significantly lower in all tested brain regions in the AD-Veh group. However, NRF1 expression was decreased to a greater extent in the cortex than other regions, while COXIV expression showed a relatively homogenous decline (**Figure 6Ae–h**, **C**, and **E**). Treatment with NSC-ex restored NRF1 and COXIV expression in multiple brain regions to levels close to those seen in WT brains, with the most striking enrichment seen in the hippocampus (**Figure 6Ai–l**, **D**, **F**, and **H**), indicating that significant protein synthesis occurs in this region. These observations are consistent with our WB results (**Figure 4C**), which showed that NRF1 expression recovered more fully than COXIV expression in the hippocampus. Moreover, significant fluorescence hyperintensities were observed in the lateral ventricles of AD-Veh and AD-ex groups (**Figure 6Ae–l**, **H**), which could be attributable to the accumulation of specific antibodies in these local cavities. Hence, NSC-ex rescue the AD-induced reduction in NRF1 and COXIV expression to varying degrees, restore their normal distribution patterns, and most noticeably affect the hippocampus.

NSC-ex suppress astrocyte activation at the whole-brain level

In the AD-Veh and AD-ex groups, we observed autofluorescence from GFAP-Cre^{+} Green. AD development is accompanied by neuroinflammation and astrocyte activation (Kaur et al., 2019). GFAP is the intermediate filament protein in astrocytes and is a recognized marker protein for astrocytes (Li et

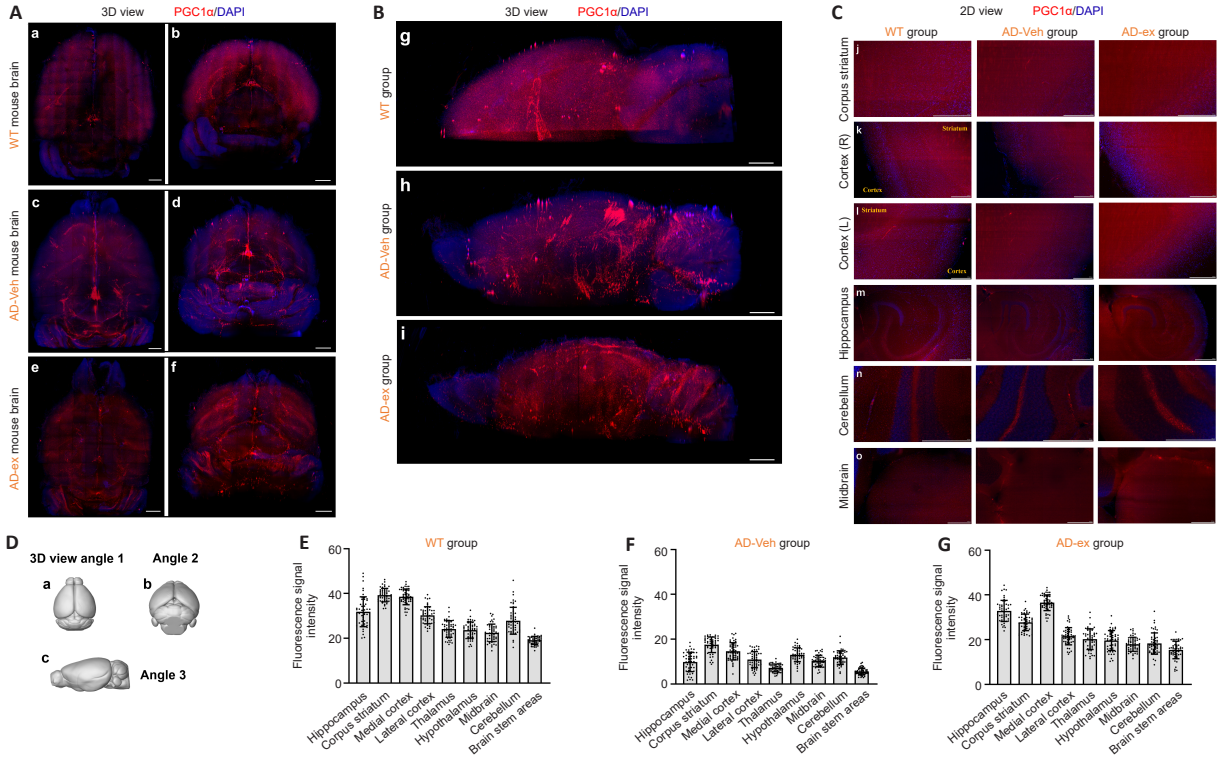

Figure 5 | **NSC-ex restore normal PGC1α distribution in the brain in an AD mouse model.**
(A and B) 3D fluorescence distribution of PGC1α (red) in the wild-type (WT), AD-Veh, and AD-ex groups. A represents the representative fluorescence images for each group of 3D views angle 1 and angle 2, and B represents the representative fluorescence images for angle 3. Three angles of the tridimensional images are presented here, namely the transverse angle (D: a [top to bottom]), the coronal angle with the head end 30 degrees upwards (D: b [back to front]), and a side view (D: c). Schematic diagram of mouse brain morphology taken from *Allen Mouse Brain* (Brain Explorer 2; Version 2.3.5 Build 2393). In the brains of WT mice (a, b, and g), PGC1α was abundantly expressed and diffusely distributed. Unlike the WT group, both the AD-Veh group (c, d, and h) and the AD-ex group (e, f, and i) showed markedly heterogeneous distributions of PGC1α throughout the brain, especially the AD-Veh group. NSC-ex treatment helped restore normal PGC1α distribution, especially in the hippocampus and cortex. (C) 2D images of PGC1α expression in the three groups in multiple brain regions, including the striatum (j), cortex (k and l), hippocampus (m), cerebellum (n), and midbrain (o). NSC-ex treatment drastically increased PGC1α expression in the medial cortex compared with that in the lateral cortex (k and l). Red fluorescence represents PGC1α, and blue fluorescence represents nuclei. (E–G) Semi-quantitative analysis of the PGC1α fluorescence in the WT group (E), AD-Veh group (F), and AD-ex group (G). Scale bars: 1 mm in A and B, 500 μm in C. WT group: Non-Tg mice WT littermates left untreated; AD-Veh group: AD mice injected with vehicle; AD-ex group: AD mice injected with NSC-derived exosomes. AD: Alzheimer's disease; NSC: neural stem cell; NSC-ex: NSC-derived exosomes; PGC1α: proliferator-activated receptor-γ coactivator-1α.

al., 2020b). The degree of up-regulation of GFAP expression represents the degree of astrocyte proliferation. Strong or weak GFAP expression reflects the functional status of astrocytes under normal or pathological conditions, respectively. We observed diffuse high-level GFAP expression in the brains of all tested AD-Veh mice, indicating that AD causes astrocyte activation at the whole-brain level, whereas treatment with NSC-ex dramatically reduced this signal (**Figure 7**). Considering the limitations of the whole-brain CUBIC assessment, which does not achieve single-cell resolution, we verified the decrease in GFAP expression after NSC-ex intervention by WB (**Additional Figure 4**).

Discussion

This study demonstrates that NSC-derived exosomes can activate SIRT1, enhance mitochondrial function, restore normal distribution of mitochondrial biogenesis-related factors (PGC1α, NRF1, and COXIV), decrease astrocyte activation, and improve cognitive function. Two AD mouse models were used in this study. In particular, compared with AD mice (APP/PS1 GFAP-Cre^{+} Green mice), SKO-AD mice (novel nervous system-specific SIRT1 conditional knockout APP/PS1 mice) showed significantly worse behavioral performance, lower levels of mitochondrial biogenesis-related factors in multiple brain regions, and higher Aβ levels, demonstrating that SIRT1 deletion causes more severe pathology and cognitive impairment. Moreover, NSC-ex treatment helped ameliorate the AD-induced abnormal distributions of PGC1α, NRF1, and COXIV at the whole-brain level, with PGC1α distribution being most markedly restored, while NRF1 and COXIV distribution patterns improved in parallel. However, NSC-ex treatment had only a slightly positive effect on Aβ levels. Our findings suggest that mitochondrial biogenesis could be a key target of the effects of NSC-ex, potentially mediated by the SIRT1-PGC1α pathway.

Exosomes carry important proteins and miRNAs, mediate essential intercellular communication and signaling pathways, and maintain environmental conditions (Kalluri and LeBleu, 2020). Previous studies have identified several components of the machinery that degrades Aβ peptides and specific surface molecules that mediate this process in extracellular vesicles or exosomes (Yuyama et al., 2014; Zhao et al., 2022). Studies have also reported that there is an intricate relationship between mitochondrial function and exosome-carried miRNAs, and that stem cell-derived exosomes confer protection from various cellular stressors via the miRNAs that they carry (Phinney et al., 2015; Fayazi et al., 2021; Hou et al., 2021). In our previous study, we reported the beneficial effects of NSC-extracellular vesicles on mitochondrial biogenesis in the cortex of APP/PS1 mice. In the present study, we explored multiple brain regions and found that NSC-ex significantly increased SIRT1 levels and mitochondrial biogenesis throughout the entire brain, not just in the cortex. Interestingly, we did not observe a significant reduction in Aβ burden in either AD mice or SKO-AD mice, indicating that NSC-ex do not primarily function via eliminating Aβ, or possibly requires longer treatment times to promote Aβ clearance. Interestingly, a recent study suggests that AD originates with faulty autolysosome acidification in neurons, rather than with Aβ deposition, indicating that Aβ deposition may be a result of, rather than a cause of, AD (Lee et al., 2022). At the cellular level, it seems likely that improving mitochondrial biogenesis or function plays a pivotal role in the NSC-ex-mediated reversal of cognitive deficits, and this process seems to involve the SIRT1-PGC1α pathways. Future studies should explore whether other exosome-related miRNA pathways also play a role.

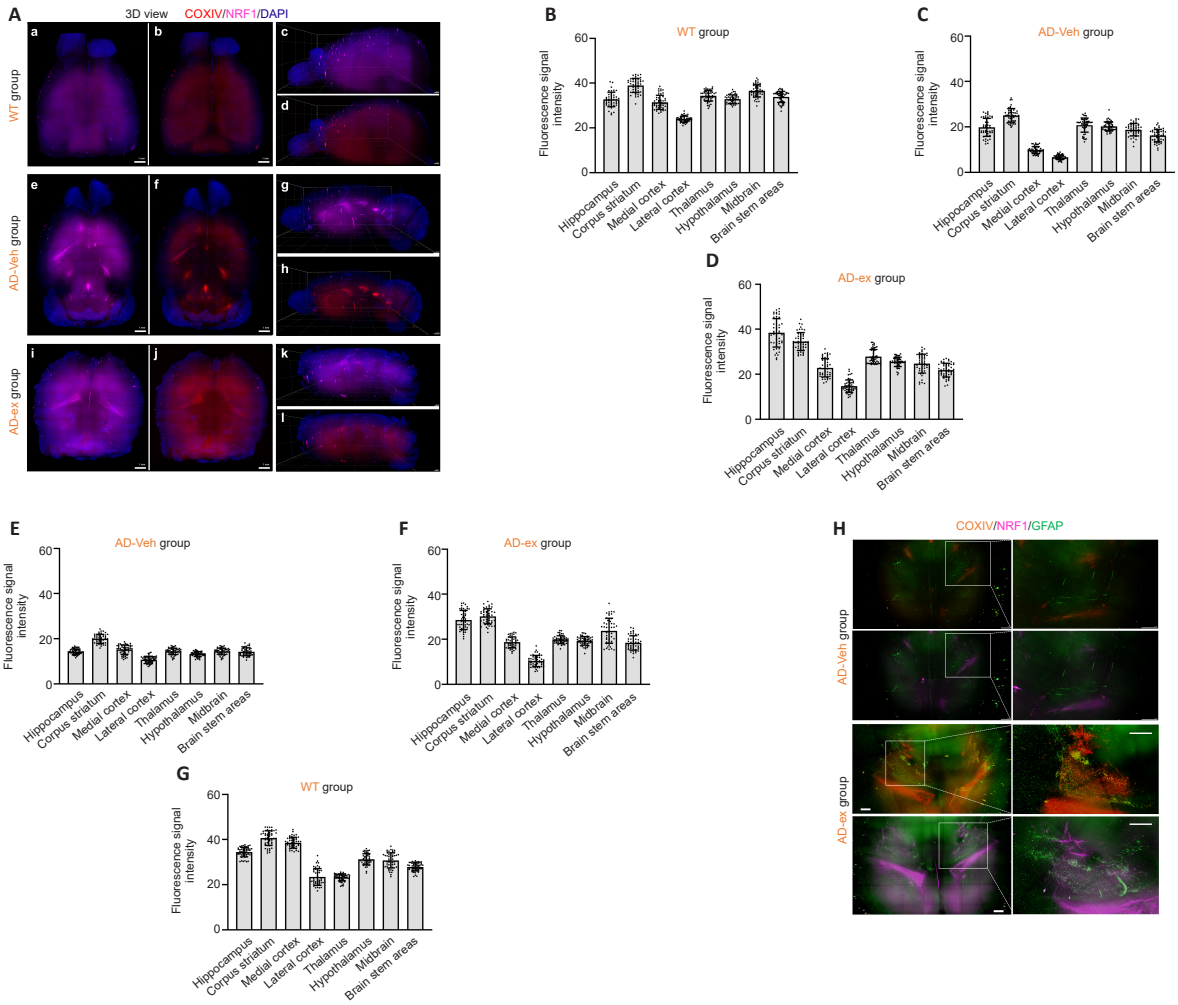

Figure 6 | **NSC-ex restore normal distribution of NRF1 and COXIV.**
(A) 3D overall fluorescence distribution of NRF1 (pink) and COXIV (red) in the WT group (a–d), AD-Veh group (e–h), and AD-ex group (i–l). The transverse angle and side angle are presented. (B–G) Fluorescence intensity analysis of NRF1 and COXIV in the three groups. NRF1 and COXIV were expressed abundantly and showed diffuse distribution, and their localization showed a high degree of overlap in the WT group. Compared with the findings in the WT group, NRF1 and COXIV expression was significantly lower in all tested brain regions in the AD-Veh group. NRF1 expression was more substantially decreased in the cortex than in other regions, while COXIV expression showed a relatively uniform decline. Treatment with NSC-ex restored NRF1 and COXIV expression in multiple brain regions to levels near those seen in the WT group, and the expression of both proteins increased most dramatically in the hippocampus. (H) NRF1 and COXIV expression levels were enriched in the hippocampus, as seen in locally magnified 3D images. Green fluorescence represents GFAP, and blue fluorescence represents nuclei. Scale bars: 1 mm in A, 500 μm in H. WT group: Non-Tg mice WT littermates left untreated; AD-Veh group: AD mice injected with vehicle; AD-ex group: AD mice injected with NSC-derived exosomes. AD: Alzheimer's disease; COXIV: cytochrome C oxidase IV; DAPI: 4′,6-diamidino-2-phenylindole; GFAP: glial fibrillary acidic protein; NRF1: nuclear respiratory factor 1; NSC: neural stem cell; NSC-ex: NSC-derived exosomes.

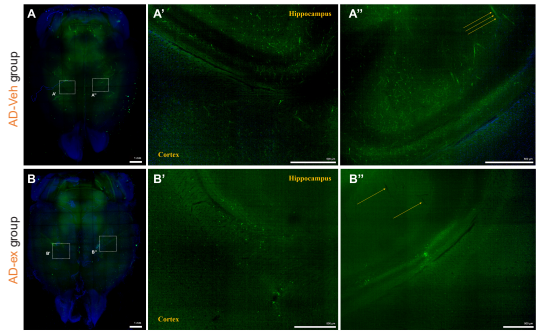

Figure 7 | **NSC-ex suppress astrocyte activation at the whole-brain level.**
Green fluorescence represents GFAP, and blue fluorescence represents nuclei. (A) Diffuse, high-level GFAP expression was observed in the brains of AD-Veh mice. A' and A'' are representative images of 2D horizontal slices. The arrows indicate vascular shadows that were apparent because of strong GFAP expression. (B) NSC-ex treatment extensively reduced GFAP expression. B' and B'' are representative images of 2D horizontal slices, similar to those selected in the AD-Veh group. Scale bars: 1 mm in A and B, 500 μm in A', A'', B', and B''. AD-Veh group: AD mice injected with vehicle; AD-ex group: AD mice injected with NSC-derived exosomes. AD: Alzheimer's disease; GFAP: glial fibrillary acidic protein; NRF1: nuclear respiratory factor 1; NSC: neural stem cell; NSC-ex: NSC-derived exosomes.

Typically, classical histology is performed on only a few selected samples, which leads to inevitable biases in the analysis of selected tissue sections and could lead to overlooking important biomedical information that is located elsewhere. By contrast, 3D histology acquired from intact, transparent specimens provides more detailed information and thus a deeper understanding of anatomy and pathophysiology. In addition, compared with classical histology approaches, 3D histology speeds up the process and reduces the cost by several thousand-fold (Ueda et al., 2020). PGC1α is a potent stimulator and sensitive indicator of mitochondrial biogenesis. PGC1α signaling stimulates NRF1 to regulate the transcription of nuclear genes encoding mitochondrial proteins, such as the mitochondrial transcription factor A, which is then transported into mitochondria and drives the expression of mitochondrial genome-encoded respiratory enzymes such as COXIV (Youle and van der Bliek, 2012; Liu et al., 2021). From a 3D perspective, we saw that PGC1α was more heterogeneously low distributed than NRF and COXIV in the brains of AD mice, indicating that PGC1α can be a more sensitive marker of mitochondrial biogenesis dysfunction. Given that NRF1 and COXIV are downstream of PGC1α, we speculate that AD most profoundly affects PGC1α, and the therapeutic effects of NSC-ex preferentially affect PGC1α over NRF1 and COXIV. Among the manifestations in multiple brain regions after NSC-ex treatment, the greatest increase in PGC1α, NRF1, and COXIV expression levels in the AD groups was observed in the hippocampus and cortex, which corresponded to the areas with the most substantial Aβ deposition in APP/PS1 mice (Burgess et al., 2006), suggesting that the beneficial effects of NSC-ex are biased towards brain regions with more severe Aβ deposition or that are more related to cognitive function.

This study had several limitations that should be noted. First, while we found that NSC-ex may act through the SIRT1-PGC1α pathway to promote mitochondrial biogenesis, the mechanism by which NSC-ex activate SIRT1 was not investigated. The specific targets and intermediate regulators between NSC-ex and SIRT1 still need to be further explored in future studies. Second, mitochondrial function is a dynamic process, and in this study, we mainly focused on mitochondrial biogenesis, so more research is needed regarding mitochondrial fusion, fission, and other aspects. In addition, although CUBIC imaging can provide global information, its cellular resolution is not yet as high as that of conventional immunofluorescence, and analysis of the extensive spatial information that it generates needs further improvement.

In conclusion, this study demonstrated the efficacy of NSC-ex in reversing cognitive deficits in two AD mouse models and investigated SIRT1 activation and regulation of mitochondria biogenesis activity during this process. We found that the SIRT1-PGC1α pathway mediates the beneficial effects of NSC-ex on mitochondrial dysfunction, and subsequently regulates NRF1 and COXIV expression. Furthermore, we found that NSC-ex restore the normal distribution of important mitochondrial biogenesis-related factors, suggesting that it could be used therapeutically to treat AD. Finally, our study shows that whole-brain/-tissue imaging provides substantial information on the spatial distribution of proteins, suggesting that it could be used for many applications.

Author contributions: *All authors have full access to all the data in the study and take responsibility for the integrity of the data and the accuracy of the data analysis, and approved the final version of the manuscript. Study concept and design: BL, QZ, WZ and JL; acquisition of data: BL, YC, XF, JL; analysis and interpretation of data: BL, YC, WZ and JL; drafting of the manuscript: BL, YC, and WZ; critical revision of the manuscript for important intellectual content: BL, YZ, and GG; statistical analysis: BL, YZ, JC and JL; obtained funding: QZ, WZ, JL; administrative, technical, and material support: YC, SH, NC and YS; study supervision: YZ, QZ, WZ and JL.*
Conflicts of interest: *The authors declare no conflicts of interest in this work.*
Data availability statement: *All data generated or analyzed during this study are included in this published article and its Additional files.*

Additional files:
Additional Figure 1: *Validation of the SKO-AD mouse model.*
Additional Figure 2: *Negative control.*
Additional Figure 3: *Sample 2D images generated from the 3D data.*
Additional Figure 4: *NSC-ex inhibited astrocyte activation.*
Additional Video 1: *A 3D representative view of PGC1α and GFAP fluorescence in AD-Veh group.*

References

Burgess BL, McIsaac SA, Naus KE, Chan JY, Tansley GH, Yang J, Miao F, Ross CJ, van Eck M, Hayden MR, van Nostrand W, St George-Hyslop P, Westaway D, Wellington CL (2006) Elevated plasma triglyceride levels precede amyloid deposition in Alzheimer's disease mouse models with abundant A beta in plasma. Neurobiol Dis 24:114-127.

Canto C, Gerhart-Hines Z, Feige JN, Lagouge M, Noriega L, Milne JC, Elliott PJ, Puigserver P, Auwerx J (2009) AMPK regulates energy expenditure by modulating NAD+ metabolism and SIRT1 activity. Nature 458:1056-1060.

Chen L, Feng Z, Yue H, Bazdar D, Mbonye U, Zender C, Harding CV, Bruggeman L, Karn J, Sieg SF, Wang B, Jin G (2018a) Exosomes derived from HIV-1-infected cells promote growth and progression of cancer via HIV TAR RNA. Nat Commun 9:4585.

Chen X, Zhou J, Li X, Wang X, Lin Y, Wang X (2018b) Exosomes derived from hypoxic epithelial ovarian cancer cells deliver microRNAs to macrophages and elicit a tumor-promoted phenotype. Cancer Lett 435:80-91.

Deng Z, Wang J, Xiao Y, Li F, Niu L, Liu X, Meng L, Zheng H (2021) Ultrasound-mediated augmented exosome release from astrocytes alleviates amyloid-beta-induced neurotoxicity. Theranostics 11:4351-4362.

Donmez G, Wang D, Cohen DE, Guarente L (2010) SIRT1 suppresses beta-amyloid production by activating the alpha-secretase gene ADAM10. Cell 142:320-332.

Dreyer F, Baur A (2016) Biogenesis and functions of exosomes and extracellular vesicles. Methods Mol Biol 1448:201-216.

Fang EF, Hou Y, Palikaras K, Adriaanse BA, Kerr JS, Yang B, Lautrup S, Hasan-Olive MM, Caponio D, Dan X, Rocktaschel P, Croteau DL, Akbari M, Greig NH, Fladby T, Nilsen H, Cader MZ, Mattson MP, Tavernarakis N, Bohr VA (2019) Mitophagy inhibits amyloid-beta and tau pathology and reverses cognitive deficits in models of Alzheimer's disease. Nat Neurosci 22:401-412.

Fayazi N, Sheykhhasan M, Soleimani Asl S, Najafi R (2021) Stem cell-derived exosomes: a new strategy of neurodegenerative disease treatment. Mol Neurobiol 58:3494-3514.

Frere S, Slutsky I (2018) Alzheimer's disease: from firing instability to homeostasis network collapse. Neuron 97:32-58.

Gomes BAQ, Silva JPB, Romeiro CFR, Dos Santos SM, Rodrigues CA, Goncalves PR, Sakai JT, Mendes PFS, Varela ELP, Monteiro MC (2018) Neuroprotective mechanisms of resveratrol in Alzheimer's disease: role of SIRT1. Oxid Med Cell Longev 2018:8152373.

Hou J, Zhang J, Cui P, Zhou Y, Liu C, Wu X, Ji Y, Wang S, Cheng B, Ye H, Shu L, Zhang K, Wang D, Xu J, Shu Q, Colonna M, Fang X (2021) TREM2 sustains macrophage-hepatocyte metabolic coordination in nonalcoholic fatty liver disease and sepsis. J Clin Invest 131:e135197.

Jagust W (2018) Imaging the evolution and pathophysiology of Alzheimer disease. Nat Rev Neurosci 19:687-700.

Jiang XH, Li HF, Chen ML, Zhang YX, Chen HB, Chen RH, Xiao YC, Liu N (2023) Treadmill exercise exerts a synergistic effect with bone marrow mesenchymal stem cell-derived exosomes on neuronal apoptosis and synaptic-axonal remodeling. Neural Regen Res 18:1293-1299.

Kalluri R, LeBleu VS (2020) The biology, function, and biomedical applications of exosomes. Science 367:eaau6977.

Kaur D, Sharma V, Deshmukh R (2019) Activation of microglia and astrocytes: a roadway to neuroinflammation and Alzheimer's disease. Inflammopharmacology 27:663-677.

Lee JH, Yang DS, Goulbourne CN, Im E, Stavrides P, Pensalfini A, Chan H, Bouchet-Marquis C, Bleiwas C, Berg MJ, Huo C, Peddy J, Pawlik M, Levy E, Rao M, Staufenbiel M, Nixon RA (2022) Faulty autolysosome acidification in Alzheimer's disease mouse models induces autophagic build-up of Abeta in neurons, yielding senile plaques. Nat Neurosci 25:688-701.

Li B, Gao Y, Zhang W, Xu JR (2018) Regulation and effects of neurotrophic factors after neural stem cell transplantation in a transgenic mouse model of Alzheimer disease. J Neurosci Res 96:828-840.

Li B, Liu J, Gu G, Han X, Zhang Q, Zhang W (2020a) Impact of neural stem cell-derived extracellular vesicles on mitochondrial dysfunction, sirtuin 1 level, and synaptic deficits in Alzheimer's disease. J Neurochem 154:502-518.

Li D, Liu X, Liu T, Liu H, Tong L, Jia S, Wang YF (2020b) Neurochemical regulation of the expression and function of glial fibrillary acidic protein in astrocytes. Glia 68:878-897.

Li H, Knight WC, Xu J (2022) Striatal oxidative damages and neuroinflammation correlate with progression and survival of Lewy body and Alzheimer diseases. Neural Regen Res 17:867-874.

Liu L, Li Y, Wang J, Zhang D, Wu H, Li W, Wei H, Ta N, Fan Y, Liu Y, Wang X, Wang J, Pan X, Liao X, Zhu Y, Chen Q (2021) Mitophagy receptor FUNDC1 is regulated by PGC-1alpha/NRF1 to fine tune mitochondrial homeostasis. EMBO Rep 22:e50629.

Liu WL, Lin HW, Lin MR, Yu Y, Liu HH, Dai YL, Chen LW, Jia WW, He XJ, Li XL, Zhu JF, Xue XH, Tao J, Chen LD (2022) Emerging blood exosome-based biomarkers for preclinical and clinical Alzheimer's disease: a meta-analysis and systematic review. Neural Regen Res 17:2381-2390.

Min SW, Cho SH, Zhou Y, Schroeder S, Haroutunian V, Seeley WW, Huang EJ, Shen Y, Masliah E, Mukherjee C, Meyers D, Cole PA, Ott M, Gan L (2010) Acetylation of tau inhibits its degradation and contributes to tauopathy. Neuron 67:953-966.

Montecalvo A, Larregina AT, Shufesky WJ, Stolz DB, Sullivan ML, Karlsson JM, Baty CJ, Gibson GA, Erdos G, Wang Z, Milosevic J, Tkacheva OA, Divito SJ, Jordan R, Lyons-Weiler J, Watkins SC, Morelli AE (2012) Mechanism of transfer of functional microRNAs between mouse dendritic cells via exosomes. Blood 119:756-766.

Pan Q, Kuang X, Cai S, Wang X, Du D, Wang J, Wang Y, Chen Y, Bihl J, Chen Y, Zhao B, Ma X (2020) miR-132-3p priming enhances the effects of mesenchymal stromal cell-derived exosomes on ameliorating brain ischemic injury. Stem Cell Res Ther 11:260.

Perez-Gracia E, Torrejon-Escribano B, Ferrer I (2008) Dystrophic neurites of senile plaques in Alzheimer's disease are deficient in cytochrome c oxidase. Acta Neuropathol 116:261-268.

Phinney DG, Di Giuseppe M, Njah J, Sala E, Shiva S, St Croix CM, Stolz DB, Watkins SC, Di YP, Leikauf GD, Kolls J, Riches DWH, Deiuliis G, Kaminski N, Boregowda SV, McKenna DH, Ortiz LA (2015) Mesenchymal stem cells use extracellular vesicles to outsource mitophagy and shuttle microRNAs. Nat Commun 6:8472.

Qiao J, Wang J, Wang H, Zhang Y, Zhu S, Adilijiang A, Guo H, Zhang R, Guo W, Luo G, Qiu Y, Xu H, Kong J, Huang Q, Li XM (2016) Regulation of astrocyte pathology by fluoxetine prevents the deterioration of Alzheimer phenotypes in an APP/PS1 mouse model. Glia 64:240-254.

Rius-Perez S, Torres-Cuevas I, Millan I, Ortega AL, Perez S (2020) PGC-1alpha, inflammation, and oxidative stress: an integrative view in metabolism. Oxid Med Cell Longev 2020:1452696.

Rong Y, Liu W, Wang J, Fan J, Luo Y, Li L, Kong F, Chen J, Tang P, Cai W (2019) Neural stem cell-derived small extracellular vesicles attenuate apoptosis and neuroinflammation after traumatic spinal cord injury by activating autophagy. Cell Death Dis 10:340.

Ryan NS, Keihaninejad S, Shakespeare TJ, Lehmann M, Crutch SJ, Malone IB, Thornton JS, Mancini L, Hyare H, Yousry T, Ridgway GR, Zhang H, Modat M, Alexander DC, Rossor MN, Ourselin S, Fox NC (2013) Magnetic resonance imaging evidence for presymptomatic change in thalamus and caudate in familial Alzheimer's disease. Brain 136:1399-1414.

Schmitz TW, Nathan Spreng R, Alzheimer's Disease Neuroimaging I (2016) Basal forebrain degeneration precedes and predicts the cortical spread of Alzheimer's pathology. Nat Commun 7:13249.

Schneider CA, Rasband WS, Eliceiri KW (2012) NIH Image to ImageJ: 25 years of image analysis. Nat Methods 9:671-675.

Susaki EA, Tainaka K, Perrin D, Yukinaga H, Kuno A, Ueda HR (2015) Advanced CUBIC protocols for whole-brain and whole-body clearing and imaging. Nat Protoc 10:1709-1727.

Tainaka K, Murakami TC, Susaki EA, Shimizu C, Saito R, Takahashi K, Hayashi-Takagi A, Sekiya H, Arima Y, Nojima S, Ikemura M, Ushiku T, Shimizu Y, Murakami M, Tanaka KF, Iino M, Kasai H, Sasaoka T, Kobayashi K, Miyazono K, et al. (2018) Chemical landscape for tissue clearing based on hydrophilic reagents. Cell Rep 24:2196-2210. e2199.

Tatulian SA (2022) Challenges and hopes for Alzheimer's disease. Drug Discov Today 27:1027-1043.

Théry C, Witwer KW, Aikawa E, Alcaraz MJ, Anderson JD, Andriantsitohaina R, Antoniou A, Arab T, Archer F, Atkin-Smith GK, Ayre DC, Bach JM, Bachurski D, Baharvand H, Balaj L, Baldacchino S, Bauer NN, Baxter AA, Bebawy M, Beckham C, et al. (2018) Minimal information for studies of extracellular vesicles 2018 (MISEV2018): a position statement of the International Society for Extracellular Vesicles and update of the MISEV2014 guidelines. J Extracell Vesicles 7:1535750.

Tomer R, Ye L, Hsueh B, Deisseroth K (2014) Advanced CLARITY for rapid and high-resolution imaging of intact tissues. Nature Protoc 9:1682-1697.

Tracy TE, Madero-Pérez J, Swaney DL, Chang TS, Moritz M, Konrad C, Ward ME, Stevenson E, Hüttenhain R, Kauwe G, Mercedes M, Sweetland-Martin L, Chen X, Mok SA, Wong MY, Telpoukhovskaia M, Min SW, Wang C, Sohn PD, Martin J, et al. (2022) Tau interactome maps synaptic and mitochondrial processes associated with neurodegeneration. Cell 185:712-728.e14.

Ueda HR, Erturk A, Chung K, Gradinaru V, Chedotal A, Tomancak P, Keller PJ (2020) Tissue clearing and its applications in neuroscience. Nat Rev Neurosci 21:61-79.

van Niel G, D'Angelo G, Raposo G (2018) Shedding light on the cell biology of extracellular vesicles. Nat Rev Mol Cell Biol 19:213-228.

Wang X, Allen M, İş Ö, Reddy JS, Tutor-New FQ, Castanedes Casey M, Carrasquillo MM, Oatman SR, Min Y, Asmann YW, Funk C, Nguyen T, Ho CC, Malphrus KG, Seyfried NT, Levey AI, Younkin SG, Murray ME, Dickson DW, Price ND, et al. (2022) Alzheimer's disease and progressive supranuclear palsy share similar transcriptomic changes in distinct brain regions. J Clin Invest 132:e149904.

Youle RJ, van der Bliek AM (2012) Mitochondrial fission, fusion, and stress. Science 337:1062-1065.

Yuyama K, Sun H, Sakai S, Mitsutake S, Okada M, Tahara H, Furukawa J, Fujitani N, Shinohara Y, Igarashi Y (2014) Decreased amyloid-beta pathologies by intracerebral loading of glycosphingolipid-enriched exosomes in Alzheimer model mice. J Biol Chem 289:24488-24498.

Zhang Q, Wu HH, Wang Y, Gu GJ, Zhang W, Xia R (2016) Neural stem cell transplantation decreases neuroinflammation in a transgenic mouse model of Alzheimer's disease. J Neurochem 136:815-825.

Zhang W, Wang PJ, Li MH, Wang GL, Li P, Gao XL (2013) 1H-MRS assessment of the therapeutic effect of bilateral intraventricular BDNF infusion into APP/PS1 double transgenic mice. J Mol Neurosci 50:434-442.

Zhao Y, Zhang J, Zheng Y, Zhang Y, Zhang XJ, Wang H, Du Y, Guan J, Wang X, Fu J (2021) NAD(+) improves cognitive function and reduces neuroinflammation by ameliorating mitochondrial damage and decreasing ROS production in chronic cerebral hypoperfusion models through Sirt1/PGC-1alpha pathway. J Neuroinflammation 18:207.

Zhao Y, Liu B, Wang J, Xu L, Yu S, Fu J, Yan X, Su J (2022) Aβ and tau regulate microglia metabolism via exosomes in Alzheimer's disease. Biomedicines 10:1800.

Zhou Y, Luo D, Shi J, Yang X, Xu W, Gao W, Guo Y, Zhao Q, Xie X, He Y, Du G, Pang X (2023) Loganin alleviated cognitive impairment in 3xTg-AD mice through promoting mitophagy mediated by optineurin. J Ethnopharmacol 312:116455.

C-Editors: Wang J, Zhao M; S-Editor: Li CH; L-Editor: Li CH, Song LP; T-Editor: Jia Y

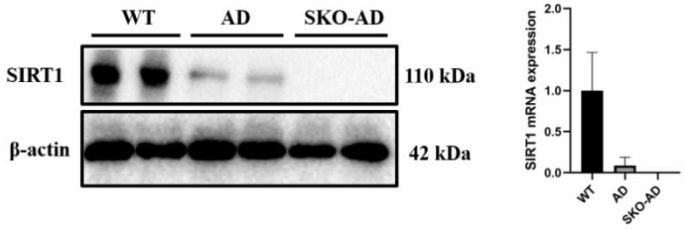

Additional Figure 1 Validation of the SKO-AD mouse model.

No significant sirtuin 1 (SIRT1) mRNA or protein expression was found in the brains of nervous system-specific SIRT1 conditional knockout APP/PS1 (APP/PS1/SIRT1 CKO [hereafter referred to as SKO-AD]) mice (*n*=5).

APP: Amyloid precursor protein; CKO: conditional knockout

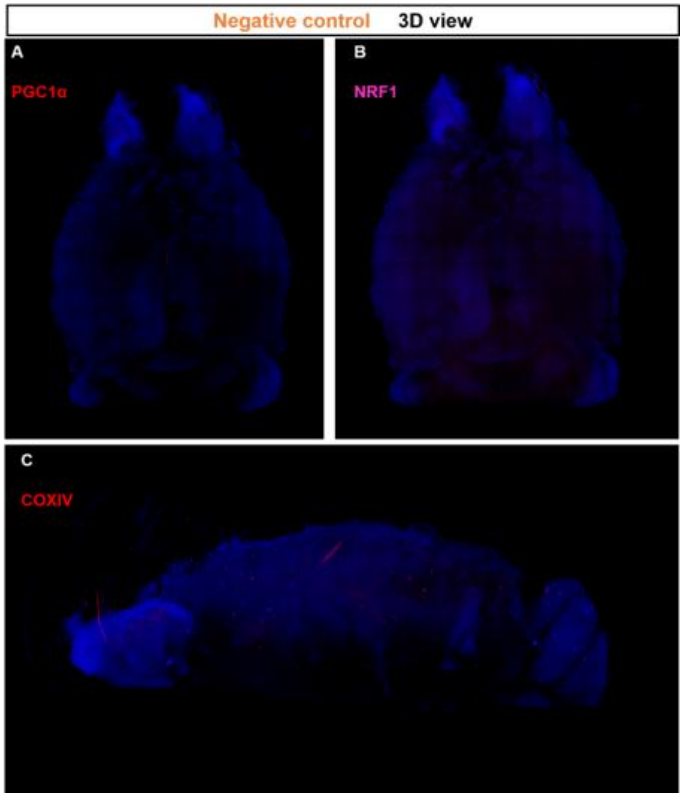

Additional Figure 2 Negative control.

Blue fluorescence represents nuclei. The negative control was imaged in the same way as the rest of the Clear, Unobstructed Brain/Body Imaging Cocktails and Computational analysis (CUBIC) imaging, without the addition of primary antibodies, to avoid possible tissue or secondary antibody autofluorescence that could lead to errors. (A) Negative control for peroxisome proliferator-activated receptor-γ coactivator-1α (PGC1α; red, with secondary antibody used). (B) Negative control for nuclear respiratory factor 1 (NRF1; pink, no antibody used). (C) Negative control for cytochrome C oxidase IV (COXIV; red, no antibody used). No obvious corresponding signals were found, demonstrating that the tissue and secondary antibody did not produce autofluorescence under normal conditions.

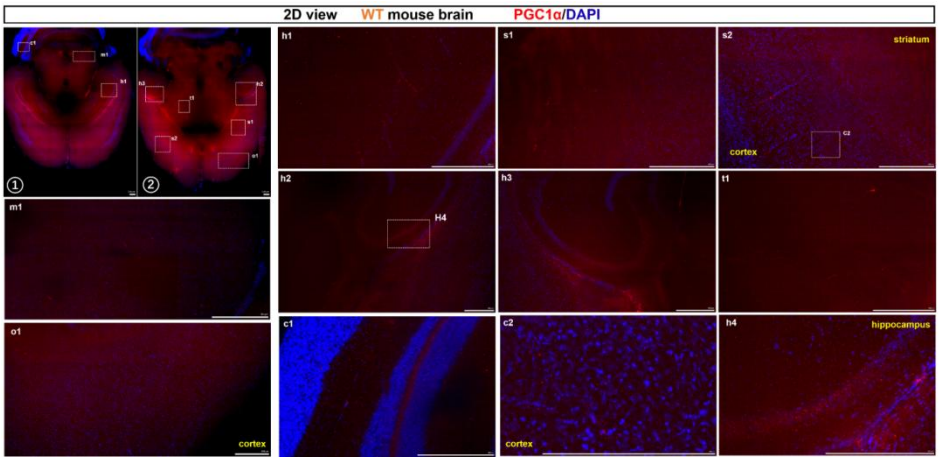

Additional Figure 3 Sample 2D images generated from the 3D data.

Red fluorescence represents peroxisome proliferator-activated receptor-γ coactivator-1α (PGC1α), and blue fluorescence represents nuclei. Images ① and ② show the fluorescence in different cross-sections of a mouse brain. Representative enlarged images show the hippocampus (h1-h4), corpus striatum (s1 and s2), thalamus (t1), midbrain (m1), cortex (s2, o1, and c2) and cerebellum (S3: c1). Scale bars: 500 μm. DAPI: 4′,6-Diamidino-2-phenylindole; WT: wild-type.

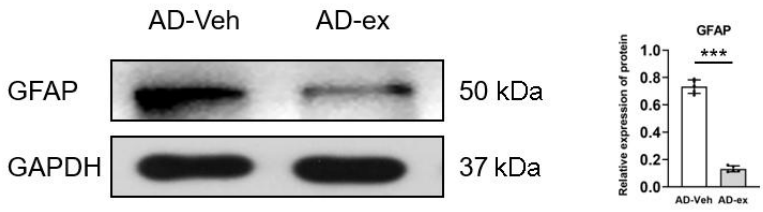

Additional Figure 4 NSC-ex inhibited astrocyte activation.

Western blot results showing that NSC-ex reduced GFAP levels. ***$P < 0.001$. AD-Veh group: AD mice injected with vehicle ($n = 15$); AD-ex group: AD mice injected with NSC-derived exosomes ($n = 15$). GAPDH: glyceraldehyde 3-phosphate dehydrogenase; GFAP: glial fibrillary acidic protein; NSC-ex: neural stem cell-derived exosomes.